

N. Kurimoto · Y. Suzuki · N. Kasagi

Active control of lifted diffusion flames with arrayed micro actuators

Received: 29 September 2004 / Revised: 15 May 2005 / Accepted: 19 June 2005 / Published online: 14 October 2005
© Springer-Verlag 2005

Abstract Active control of a lifted flame issued from a coaxial nozzle is investigated. Arrayed micro flap actuators are employed to introduce disturbances locally into the initial shear layer. Shedding of large-scale vortex rings is modified with the flap motion, and the flame characteristics such as liftoff height, blowoff limit, and emission trend, are successfully manipulated. Spatio-temporal evolution of large-scale vortical structures and fuel concentration is examined with the aid of PIV and PLIF in order to elucidate the control mechanisms. It is found that, depending on the driving signal of the flaps, the near-field vortical structures are significantly modified and two types of lifted flames having different stabilization mechanisms are realized.

1 Introduction

Small-scale distributed generation (DG) systems are expected to establish the future energy security as well as to solve the environmental issues. Micro gas turbine having 1–100 kW power generation is one of the central elements of the systems (e.g. Uechi et al. 2004). Unlike large-scale power plants, micro gas turbine is operated at a wide range of partial loads. Therefore, in order to make micro gas turbine highly competitive in the future DG systems, it is necessary to develop small-scale highly efficient combustors which ensure stable and low-emission flame under any possible operating conditions.

Recently, smart control of turbulent shear flows has attracted much attention. Since large-scale coherent

structures emerging in various shear flows play a dominant role in turbulent transportation (e.g. Cantwell 1981), selective manipulation of those structures is desired in order to obtain efficient control effect. Recent development of micro electro-mechanical systems (MEMS) technology enables us to fabricate micro actuators for flow control, which are small enough to introduce control input directly into the shear layers (e.g. Ho and Tai 1996). For combustion control, it is a technological challenge to develop an actively controlled burner which makes it possible to keep stable and low-emission flame under any operating conditions.

Lifted flame is a typical form of flame in industrial combustors. Flamed fuel jet surrounded by an annular airflow forms a diffusion flame. The flame is held by the burner rim when the fuel/air velocity is small enough. If the velocity is larger than a critical value, but smaller than the blowoff limit, the flame is lifted at a certain downstream distance from the rim. In designing industrial burners, it is of practical importance to predict the flame characteristics such as the liftoff height and the liftoff/blowoff velocity limits.

Many studies on lifted flame have focused on predicting these features through modeling the stabilization mechanism (Pitts 1988). Vanquickenborne and Tiggelen (1966) hypothesized that fuel is well premixed with air upstream and the turbulent burning velocity balances with the flow velocity at the flame base. Based on these assumptions, they derived an empirical relation between the turbulent burning velocity and characteristics of turbulence. On the other hand, Peters and Williams (1983) assumed that the liftoff process is controlled by the quenching of laminar diffusion flamelets, which is determined by a local scalar dissipation rate. They showed that the liftoff height estimated by the assumption is in good agreement with experimental results. Recently, it is considered that fuel and air are partially premixed upstream of the flame base and that a laminar triple flame plays a dominant role in the flame stabilization mechanism (Vervisch 2000). Muñiz and Mungal (1997) measured instantaneous, two-dimensional velo-

N. Kurimoto · Y. Suzuki (✉) · N. Kasagi
Department of Mechanical Engineering, The University of Tokyo,
Hongo 7-3-1, Bunkyo-ku, Tokyo 113-8656, Japan
E-mail: kurimoto@thtlab.t.u-tokyo.ac.jp
E-mail: ysuzuki@thtlab.t.u-tokyo.ac.jp
Tel.: +81-3-58416411
Fax: +81-3-58006999
E-mail: kasagi@thtlab.t.u-tokyo.ac.jp

city field near the flame base by using particle image velocimetry (PIV). They found that the instantaneous flame shapes and the velocity profiles are similar to those predicted by the numerical simulation of triple flames. They also found that the lifted flame blows off when the air velocity is more than three times larger than the laminar burning velocity.

Role of large-scale vortices in the flame-holding process is also of great interest. Everest et al. (1996) discussed the effect of vortex rings on the stabilization mechanism, based on the simulations of Ashurst and Williams (1990). They experimentally visualized the flammable layer and the scalar dissipation rate for a cold propane jet. They showed that, at the location of the flame base, the flammable layer becomes significantly thin in the downstream portion of the large-scale vortex, where the dissipation rate is large enough to extinguish the diffusion flamelet. On the other hand, in the upstream portion of the vortex, the flammable layer thickens engulfed in the vortex, and the dissipation rate becomes small enough to allow the flame propagation. Chao et al. (2002) measured the phase-averaged distribution of OH and H₂O at the flame base of the lifted flame tuned by acoustic excitation, and discussed the stabilization process associated with cyclically incoming vortices. They proposed one cycle of flame stabilization as follows. First, the flame propagates the flammable layer upstream and is extinguished by the extensive strain in the downstream portion of the incoming vortex. Second, when the vortex breaks down and the strain weakens, the flame restarts to propagate upstream.

The stabilization mechanism is investigated in further details with the recent development of laser techniques. Schefer and Goix (1998) examined a turbulent lifted flame under various Reynolds numbers with PIV and planar laser-induced fluorescence (PLIF) of OH radical. They found that, at the flame base, the mixture is close to the stoichiometric condition and the flow velocity is small enough to allow the leading-edge flame to propagate upstream. Su et al. (2000) made a simultaneous measurement of PIV and LIF for the lifted flame base, and examined the velocity and the fuel mole fraction. They reported that the fuel concentration at the leading point is within the flammable limits and the leading-edge flame is held interacting with the incoming vortices. In addition to the measurement of the vertical plane, Demare and Baillot (2001) performed high-speed laser tomography in the transverse plane and examined the role of the streamwise vortices in the flame stabilization. They reported that the streamwise vortices enhance the fuel-air mixing in smaller scales than the large-scale ring vortices and play a dominant role in the flame stabilization.

It is well known that perturbations in the jet shear layers are amplified through shear layer and/or column-mode instabilities and roll up into large-scale vortices (Hussain and Zaman 1981). Since the development of the vortices is susceptible to the acoustic perturbations, artificially generated perturbations have

been extensively employed to alter the structures or enhance turbulent mixing (Crow and Champagne 1971; Zaman and Hussain 1980; Ho and Huerre 1984). Chao and Jeng (1992) excited a propane/air premixed lifted flame at its preferred-mode frequency with an acoustic speaker. They reported that the excited vortical structure decreases the liftoff height. Baillot and Demare (2002) systematically investigated the effect of the forcing frequency and amplitude on acoustically excited lifted flames, and showed that the acoustic perturbations either prevent reattachment of the flame to the burner and enhance combustion, or weaken the flame stability. In addition to the axisymmetric forcing, Chao et al. (2000) employed a control nozzle equipped with eight piezoelectric actuators around the exit in order to introduce helical-mode disturbances. They showed that the helical-mode excitation intensifies one of the streamwise vortices right upstream of the flame base, and the flame base is inclined to the nozzle exit. This is because the intensified streamwise vortex provides an additional path for the flame propagation through the enhancement of mixing.

Emission of nitrogen oxides (NO_x) and unburnt hydrocarbons (UHC) is also of great interest. Fujimori et al. (1998) investigated relationship between NO_x emission and liftoff height of methane diffusion flames in high temperature airflows. They showed that the NO_x emission is reduced significantly if the liftoff height is larger than the attached flame length. This is because the complete mixing is accomplished upstream of the flame base and lean mixture is supplied to the flame. Chao et al. (1996) examined NO_x and UHC emissions in propane/air premixed lifted flame excited with an acoustic speaker. They reported that mixing between the premixture and ambient air is enhanced upstream of the flame base, and that NO_x emission is reduced without the significant increase of UHC.

Suzuki et al. (1999, 2004) developed micro magnetic-flap actuators and arranged 18 flaps on the inner wall of a round nozzle in order to manipulate the near-field vortical structures. They realized a furcating jet by modulating the azimuthal phase of the disturbances introduced into the jet shear layer. Kurimoto et al. (2001) applied the flap actuators to an axisymmetric coaxial nozzle. They manipulated the near-field vortical structures of the coaxial jet and achieved drastic enhancement of the mixing. It is expected that the manipulation of the near-field vortical structures by the flap actuators could also alter the characteristics of coaxial jet flames.

The objectives of the present study are to develop an active control scheme of coaxial jet flames and to examine the effect of selective manipulation of the near-field vortical structures on the lifted flame. For this purpose, we employ the flap actuators (Suzuki et al. 1999, 2004) in an axisymmetric coaxial nozzle. In order to examine the spatio-temporal evolution of large-scale vortical structures, we employ two-component (2-C) PIV and PLIF.

2 Experimental setup

2.1 Coaxial nozzle and flap actuator

Axisymmetric coaxial jet nozzle employed in the present study is shown in Fig. 1a. The annular nozzle has an inner diameter D_o of 20 mm at the exit with a contraction area ratio of 42. The central jet is issued from a straight tube having an inner diameter D_i of 10 mm and a wall thickness of 0.3 mm. The length of the tube is 1 m, which is long enough for a fully developed laminar flow to be established. The inner diameter ratio $\beta (= D_o/D_i)$ is 2. A total of 18 flap actuators (Suzuki et al. 1999, 2004) are arranged on the inner wall of the outer nozzle lip, which cover 86% of the circumference. In the present study, all flaps are driven in phase. Dahm et al. (1992) and Rehab et al. (1997) separately showed that the near-field vortical structures of coaxial jets are dominated by the vortices emerging in the outer shear layer when the annular flow velocity is larger than the central one. Therefore, we introduce the control input into the outer shear layer in order to manipulate the vortical structures effectively.

The flap actuator is made of a copper plated polyimide film of 9 mm in length and 3 mm in width (Fig. 1b). Thickness of the polyimide and copper layer is

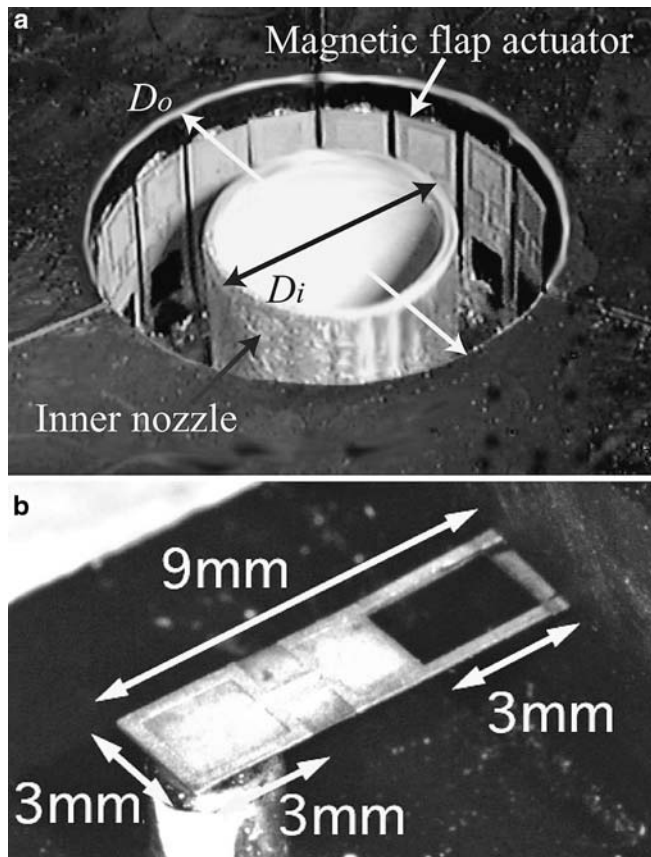


Fig. 1 (a) Coaxial nozzle equipped with 18 magnetic flap actuators, (b) magnetic flap actuator (Suzuki et al. 2004)

both 35 μm . A single-turn coil is patterned on the copper layer using photolithography (Suzuki et al. 1999, 2004). When an electric current is applied to the copper coil, the flap is elastically bent by the magnetic force generated between the coil and a cylindrical permanent magnet embedded in the nozzle wall. The resonant frequency of the flap actuator is 310 Hz. In the present study, all the flaps are driven by an alternating current, and their motion is in-phase. In a preliminary experiment, four kinds of driving signals (sinusoidal-, triangle-, saw-, and square-wave) were examined. In the present study, the saw-wave and square-wave driving signals are employed, since characteristics of lifted flames are markedly modified with those signals. The power consumption is, respectively, 0.2 and 0.5 W for the saw- and square-wave signals, which is negligibly smaller than the heat release rate in the present flame (~ 3.5 kW).

Dynamic response of the actuator is examined with a laser displacement meter (Keyence, LC-2440). Figure 2 shows time trace of the flap deflection at the center of the coil for the saw- and square-wave driving signals at 95 Hz. The initial position of the flap is in contact with the magnet, so that the flap can only move away from the wall. When the flap is driven with the saw-wave signal, it is repelled from the magnet following the driving signal (Fig. 2a). The displacement includes the resonant-frequency oscillation, but its amplitude is small. After reaching the maximum displacement of 0.3 mm, it snaps quickly back to the wall on the trailing edge of the signal. On the other hand, when the square-wave signal is employed, the flap is quickly repelled from the magnet following the leading-edge of the signal (Fig. 2b). After reaching the maximum displacement of

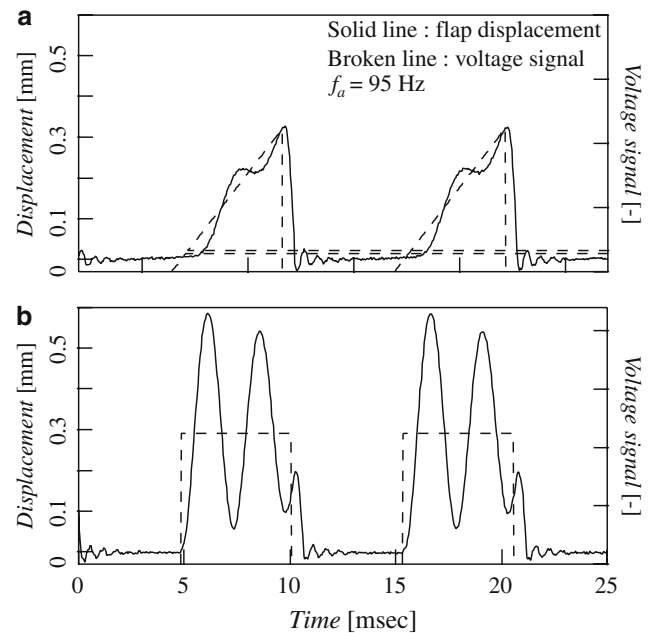


Fig. 2 Time trace of a flap actuator deflection. (a) Saw-wave and (b) square-wave driving signal

0.6 mm, it exhibits the damping oscillation at the resonant frequency, and the oscillation lasts until the flap is pulled back to the initial position. The power consumption of each mode is 0.2 and 0.5 W for the saw- and square-wave signals, respectively, which is negligibly smaller than the heat release rate in the present flame (~ 3.5 kW).

2.2 Flow facility

Schematic of the experimental setup is shown in Fig. 3. The central and annular flows are methane and air, respectively. The methane is supplied from a compressed gas container. The air is supplied from a compressor and goes through a dehumidifier (SMC, IDG10V-02) to keep the dew point of the air below 253 K. Then, the air is introduced into a plenum chamber with a honeycomb and several meshes. Flow rates of both streams are independently measured with mass flow meters (Yamatake, CMQ series). The coaxial jet is discharged vertically into ambient air, which is surrounded by four plates of wind shields. Each plate has a quartz window, which provides optical access for a laser sheet and image acquisition. The test section is 1,000 mm in height with a square cross-section of 560×560 mm². Hereafter, the cylindrical coordinate system is employed, where x, r , and θ are the streamwise, radial, and azimuthal directions, respectively.

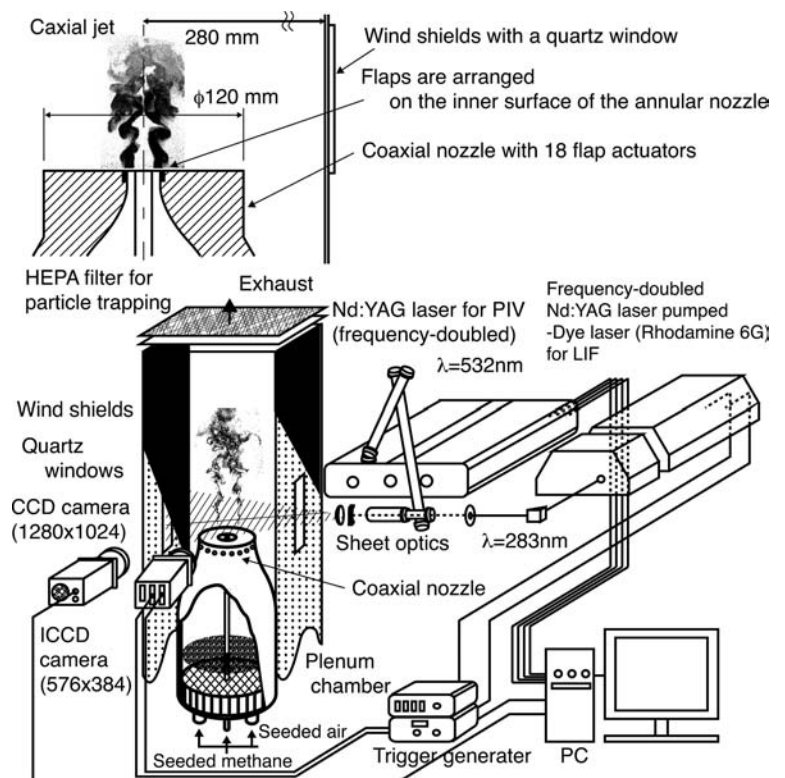
In representative results of the flame control described later, the bulk mean velocities of the inner and

annular flows are, respectively, $U_{m,i} = 1.2$ m/s and $U_{m,o} = 1.8$ m/s, which corresponds to a 3.5 kW diffusion jet flame. The Reynolds number $Re (= U_{m,o} D_o / \nu_o)$ is 2.4×10^3 . The momentum flux ratio $m (= \rho_o U_{m,o}^2 / \rho_i U_{m,i}^2)$, which plays a dominant role on the dynamics of coaxial jets (Favre-Marinet and Camano Schettini 2001), is 4. Hereafter, these values are employed unless otherwise noted. Exit velocity profile is measured with a two-component fiber LDV (Dantec, 60 \times 11) with a measurement volume of $x \times r \times \theta = 78 \times 659 \times 78$ mm³. Figure 4 shows the radial profiles of the streamwise mean velocity and turbulent intensity at the nozzle exit. The mean velocity profile of the central jet is parabolic, and the turbulent intensity is approximately constant to be 0.05. On the other hand, turbulent intensities in the outer potential core and the shear layers are somewhat large, and, respectively, 0.1 and 0.2.

2.3 Velocity measurement

Two-component PIV is employed for the velocity measurement. The inner and outer jets are seeded with silica particles ($d_p = 1.2$ μ m, $\rho_p = 215$ kg/m³). The particle relaxation time τ_p is approximately 1 μ s (Melling 1997), which is much smaller than the Kolmogorov time scale $\tau_s \sim 222$ μ s estimated by $D_o^2 Re^{-3/2} \nu_{air}$. Before introducing into the nozzles, the inner and outer flows are bisected, and one of a pair is introduced into a seeding system, and is recombined with the bypassed flow. The seeding system consists of a vessel filled with the

Fig. 3 Schematic of experimental setup



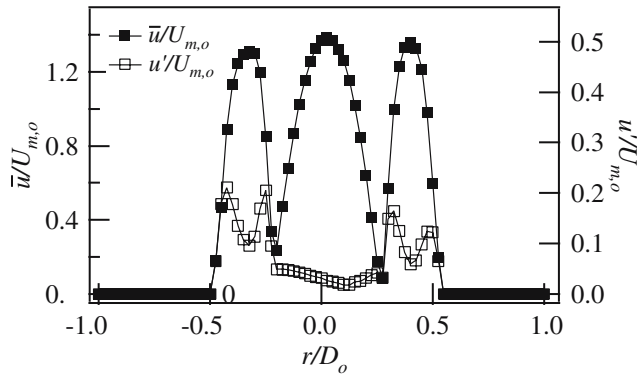


Fig. 4 Radial distribution of the mean velocity and turbulent intensity at $x/D_o = 0.025$

particles, which are agitated and suspended by a magnetic stirrer.

A double-pulsed Nd:YAG laser (THALES, SAGA PIV20, 400 mJ/pulse at 532 nm) is employed for the light source. The laser beam is formed into a sheet (~ 1 mm thick) through several cylindrical lenses and introduced into the test section. Particle images are captured by a frame-straddling CCD camera (Lavis, FlowMaster3, $1,280 \times 1,024$ pixels²) equipped with a Nikon 50 mm f/11 lens. The field of view is 56×45 mm². Commercial software (Lavis, Davis 6.2) is used to calculate the average particle displacement in an interrogation area with a cross-correlation technique. The size of the interrogation area is 32×32 pixels², which corresponds to a physical dimension of 1.4×1.4 mm². The images are processed to yield 80×64 vectors with 50% overlap in each direction. Interrogation areas where the correlation ratio between the first and second peaks is smaller than 1.3 are rejected as spurious velocity (Kean and Adrian 1990). The time interval of the laser pulses is chosen as 50 μ s in order to minimize the unwanted effect of the velocity gradient in the shear layer (Kean and Adrian 1992). The yield of the velocity vectors thus obtained is more than 95%. The uncertainty interval estimated at 95% coverage by the method of ANSI/ASME PTC (1985) is $0.07 U_{m,o}$ for the instantaneous velocity. The precision index and the bias limit are $0.02 U_{m,o}$ and $0.06 U_{m,o}$, respectively.

2.4 Scalar measurement

Scalar mixing process is investigated through PLIF. The inner methane flow is seeded with acetone vapor by bubbling the carrier gas into a liquid acetone container (Lozano et al. 1992). Stable seeding is achieved once thermal equilibrium is reached. The acetone temperature is approximately 291 K, which corresponds to the partial pressure of 2.4×10^4 Pa. Acetone vapor is excited by a frequency-doubled pulsed dye laser, which is pumped by a doubled Nd:YAG laser (Lamda Physik, SCANmate).

Rhodamine 6G dye is chosen to produce 283.0 nm UV light pulses of 10 mJ/pulse. The laser beam is introduced into the test section through a quartz window and formed into a laser sheet of 0.4 mm thickness, which results in intensity of 1.4 mJ/cm. An image-intensified CCD camera (LaVision, Flamestar2) of 576×384 pixels² is employed for image acquisition. The ICCD camera is equipped with a 100 mm UV lens as well as a low-pass optical filter having a cutoff wavelength of 295 nm in order to eliminate the Mie scattering of the laser sheet from dust particles. The field of view is set to be 60×40 mm². In order to reduce the effect of shot noise, fluorescence signals in a subregion of 4×4 pixels² are ensemble-averaged. The resultant spatial resolution is 0.4×0.4 mm², which is somewhat larger than the Kolmogorov length scale estimated to be $D_o Re^{-3/4} = 0.06$ mm.

Fluorescent intensity at each pixel is converted to the instantaneous normalized scalar concentration by

$$\tilde{\chi}_f = \frac{\tilde{c}}{\tilde{c}_o} = \frac{[I_{FL}(x, r) - I_{BG}(x, r)] / [I_{ref}(x) - I_{BG}(x, r)]}{\langle [I_{FL}(x, r) - I_{BG}(x, r)] / [I_{ref}(x) - I_{BG}(x, r)] \rangle_o}, \quad (1)$$

where I_{FL} , I_{ref} , and I_{BG} are, respectively, the raw fluorescent intensity, the reference image intensity and the background intensity. The bracket $\langle \rangle_o$ represents a spatial average in the jet potential core. Intensity of each laser pulse is evaluated through averaging the fluorescence signals in the potential core, and its fluctuation is compensated. Spatial inhomogeneity of the laser pulse energy is also compensated with the reference image. The reference image is taken by introducing laser sheet into a quartz container filled with acetone vapor. The linearity of the fluorescent intensity to the acetone concentration and incident light intensity is ensured in a preliminary experiment. Taking account of the shot noise in the weak light detection, the uncertainty interval estimated at 95% coverage is 0.015 for the instantaneous concentration of $\tilde{\chi}_f = 0.1$.

The mixture fraction of methane is estimated from the LIF images, where the acetone vapor is seeded into the inner methane flow. Based on an assumption that the distribution of the acetone vapor equals that of the methane, the mixture fraction is calculated as follows:

$$\tilde{Z} = \frac{\tilde{\chi}_f M_f}{\tilde{\chi}_f M_f + (1 - \tilde{\chi}_f) M_a}, \quad (2)$$

where M_f and M_a are, respectively, the molecular weights of methane and air.

Characteristic diffusion length scale based on the binary diffusion coefficient of methane in air ($\alpha_1 = 0.22$ cm²/s) is estimated to be $\Delta_1 = (\alpha_1 D_o / U_{m,o})^{0.5} \sim 0.5$ mm, while that based on diffusivity of acetone in air ($\alpha_2 = 0.10$ cm²/s) is $\Delta_2 \sim 0.3$ mm. Since length scales are comparable to the spatial resolution of the image, the use of Eq. 2 for calculating the fuel mixture fraction is justified.

2.5 Exhaust gas analysis

The sampling point is located on the jet axis at $x/D_o = 28$, which is approximately two flame-lengths downstream as suggested by Drake et al. (1987). At the location, the combustion gas is diluted and cooled by mixing with the ambient air, so that chemical reactions are considered to be frozen. A stainless tube with the diameter of 10 mm is used for gas sampling. The overall exhaust gas is extracted continuously at the flow speed of 0.2 m/s, which is slow enough to ensure that the upstream flame is not significantly disturbed. In order to eliminate moisture and soot, the sampled gas is introduced into the pre-processing sampling unit (Shimadzu, CFP-8000) through a Teflon line, and collected in a 20-l Teflon bag. The sampling bag is then connected to an oximeter (Horiba, MEXA-4001) and an exhaust gas analyzer (Horiba, MEXA-4000FT) to measure NO_x and CO. The amount of emissions is evaluated as volumetric fractions at 15% O_2 . The uncertainty interval is approximately 10 ppm as shown later.

3 Cold jet control

3.1 Visualization

Instantaneous LIF images of the natural and controlled cold jets are shown in Fig. 5, where acetone vapor is separately seeded in the inner or outer flow. As shown in Fig. 5a, b the inner and outer shear layers in the natural jet start to roll up into large-scale vortices at $x/D_o \sim 2$ through the column-mode instability (Hussain and Zaman 1981). The preferred-mode frequency f_p of the vortex shedding is 57 Hz, which corresponds to the Strouhal number $St_p (= f_p D_o / U_{m,o})$ of 0.62.

On the other hand, in the controlled jet with the saw-wave signal (Case 1), the outer shear layer is forced to roll up into large-scale intense vortices in phase with the flap motion, and the vortices pinch off the inner jet significantly (Fig. 5c, d). It is found that the vortex shedding is independent of the column-mode instability, and intense vortices are shed perfectly in phase with the flap motion even if the flapping frequency f_a is much smaller than f_p . Therefore the flapping frequency is chosen at $f_a = 95$ Hz ($St_a = f_a D_o / U_{m,o} = 1.0$) which is the optimum frequency for flame stabilization as shown later.

Figure 5e, f show the controlled jet with the square-wave signal at the same flapping frequency (Case 2). Unlike Case 1, the distinct roll-up of the tracer is not observed in the outer shear layer.

3.2 Vortical structures and mass transfer

In this section, vortical structures are examined in detail by phase-locked measurements. Instantaneous velocity vector \vec{u} and mixture fraction \tilde{Z} are, respectively, decomposed as follows:

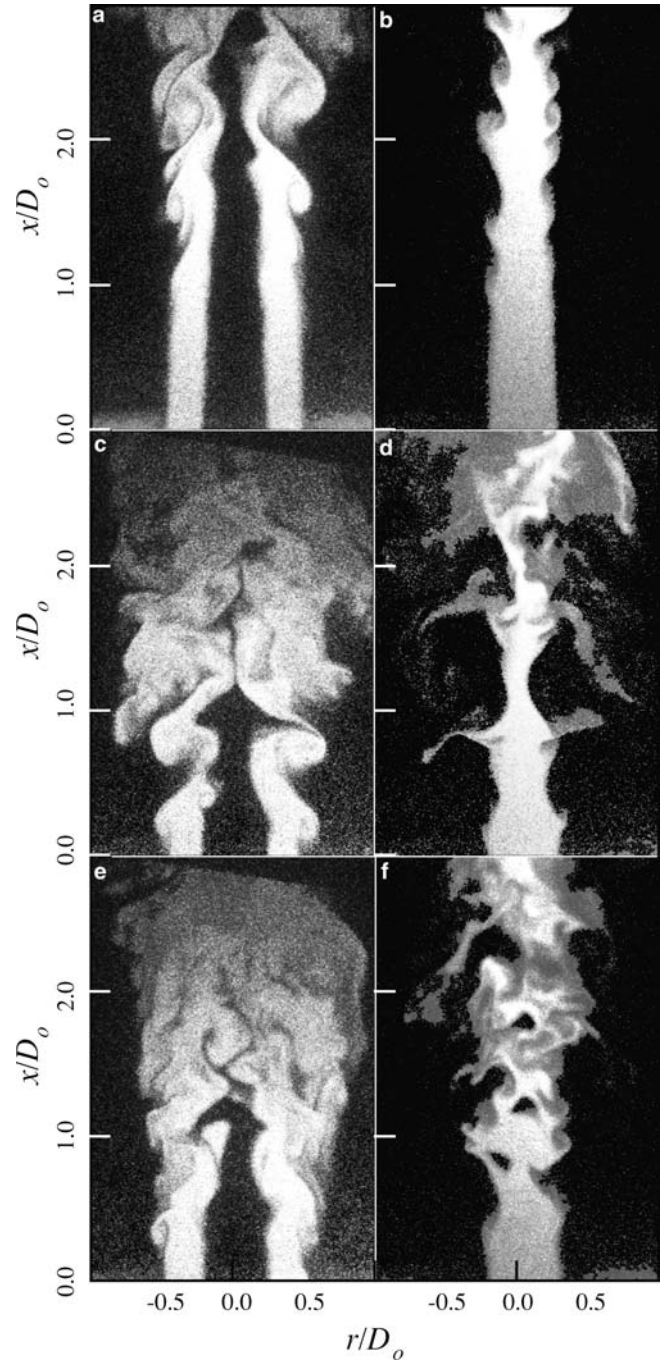


Fig. 5 Instantaneous images of the outer and inner jets. (a, b) Natural, (c, d) Case 1 (saw-wave signal, $St_a = f_a D_o / U_{m,o} = 1.0$), (e, f) Case 2 (square-wave signal, $St_a = 1.0$)

$$\vec{u} = \bar{\vec{u}} + \vec{u}_\phi + \vec{u}' \quad (3)$$

$$\tilde{Z} = \bar{Z} + Z_\phi + Z' \quad (4)$$

The first, second, and last terms of the right-hand sides, respectively, correspond to the mean, phase-averaged and fluctuating components. Figure 6 shows \vec{u} , $(\vec{u}_{\phi=\pi} + \vec{u}')$, $\sqrt{\vec{u}'^2}$ and $\vec{u}_{\phi=\pi}$ in the controlled jet.

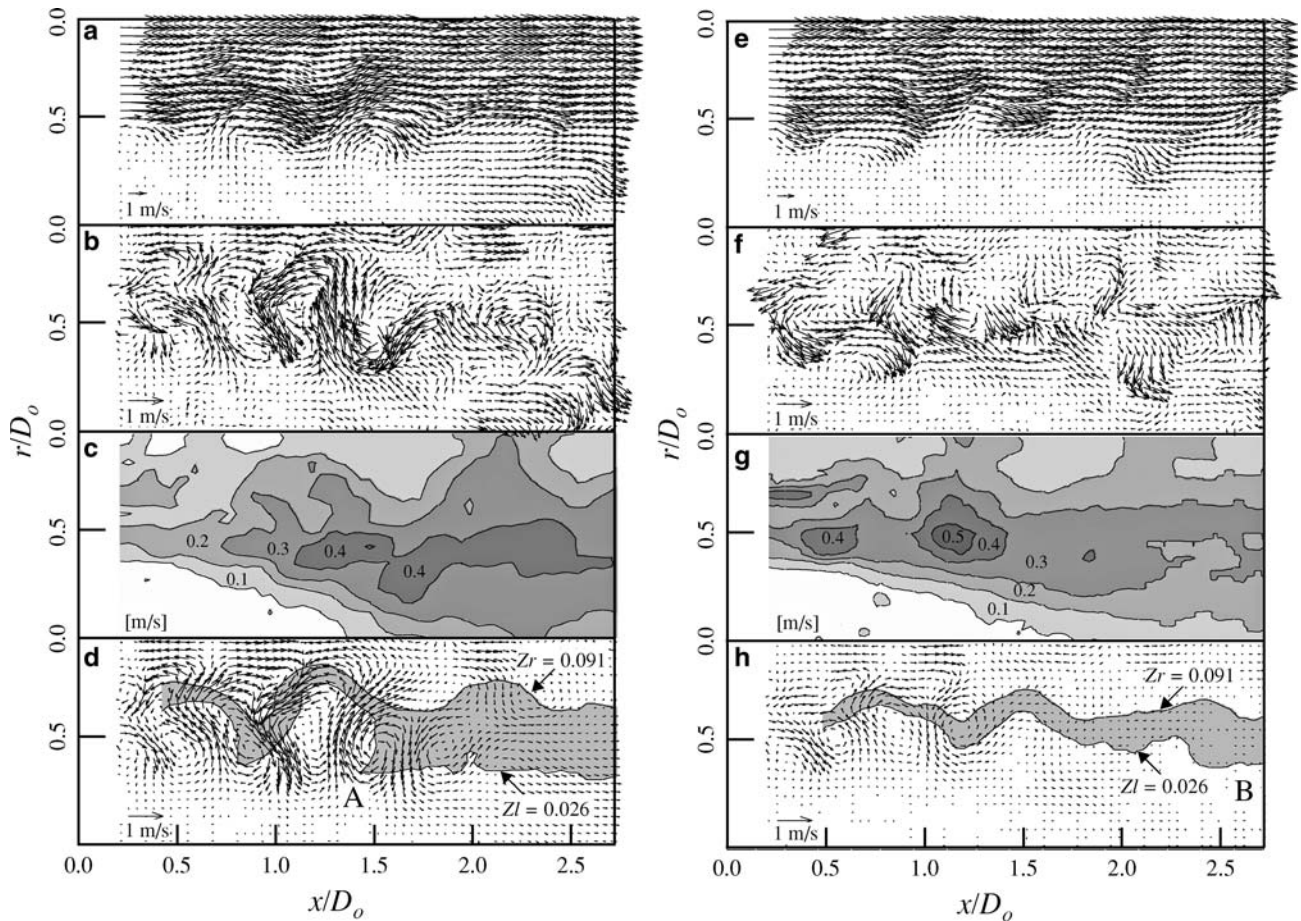


Fig. 6 Velocity vectors and scalar fields for the controlled jets with $St_a = 1.0$ for (a–d) Case 1, and (e–h) Case 2. Image acquisition is locked at $\phi = \pi$. (a, e) \vec{u} , (b, f) $(\vec{u}_\phi + \vec{u}')$, (c, g) $\sqrt{\vec{u}'^2}$ (d, h) \bar{u}_ϕ and contours of rich and lean flammable limits of $(\bar{Z} + Z_\phi)$

Contours of the rich and lean flammable limits of the mixture fraction $(\bar{Z} + Z_{\phi=\pi})$, that is, $Z_r = 0.091$ and $Z_l = 0.026$, are also depicted on Fig. 6d, h.

In Case 1, large-scale intense vortices are periodically produced by the flaps and densely populated near the nozzle exit as shown in Fig. 6a, b. Magnitude of $\sqrt{\vec{u}'^2}$ is small near the nozzle exit, while it increases downstream until reaching a peak at $x/D_o = 1.0 \sim 1.5$ as shown in Fig. 6c. This means that those vortices are intense and remain axisymmetric at $x/D_o < 1.5$, while they breakdown into turbulence further downstream. The large-scale vortex in the near-field enhances the radial transport of the inner fluid, and engulfs the flammable region toward the jet axis (Fig. 6d). At $x/D_o < 1.5$, the flammable region is localized near the vortex, while it is distributed extensively further downstream due to the breakdown of the vortex.

On the other hand, in Case 2, large-scale vortical structures are less ordered than in Case 1 (Fig. 6e, f) and $\sqrt{\vec{u}'^2}$ becomes large at $x/D_o \sim 0.5$ (Fig. 6g). This means that the large-scale vortices in the outer shear layer break into turbulence near the nozzle exit. Because of

the early breakdown of the vortices, the radial transport of the inner fluid becomes smaller, and the flammable region is much thinner than that of Case 1 (Fig. 6h).

Figure 7 shows the instantaneous cross-sectional images of the controlled jet of Case 1 at $x/D_o = 1.5$. Acetone vapor is separately seeded in the outer or inner flow. It is found that streamwise vortical structures are formed in the outer mixing layer (Fig. 7a), and the inner fuel transported outward by the primary vortex upstream is trapped in the structures (Fig. 7b). These structures are considered to originate from the braid region of the large-scale vortical structures near the nozzle exit (Liepmann and Gharib 1992). In Case 2, those structures were not observed as clearly as in Case 1. It is probably because the large-scale vortices are broken down into turbulence near the nozzle exit.

4 Lifted flame control

4.1 Flame observations

Instantaneous images of the natural and controlled lifted flames are shown in Fig. 8. Smoke is introduced into the

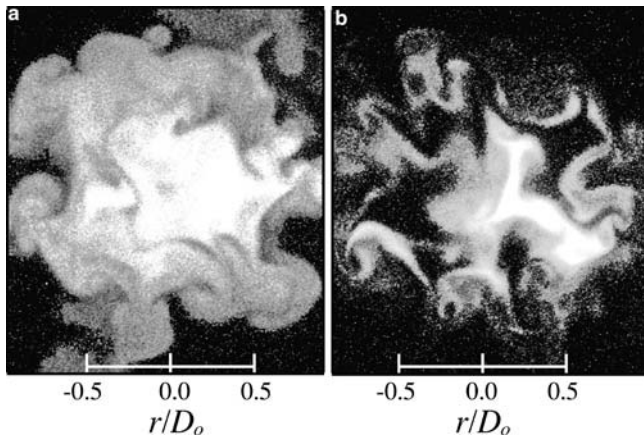


Fig. 7 Instantaneous cross-sectional images of the controlled jet with Case 1 at $x/D_o = 1.5$. (a) Outer airflow and (b) inner fuel flow

annular airflow, and the image is captured together with luminescence of the flame. As shown in Fig. 8a, flame base of the natural flame is located near the end of the inner potential core, but the lifted flame is unstable and easily blows off. This is probably because quasi-periodic passage of the vortices emerging at the potential core end significantly disturbs the flame propagation.

On the other hand, the controlled flames become stable for both controlled cases. In Case 1, the large-scale vortices produced by the flaps are clearly observed at the flame base, and the flame is anchored at $x/D_o \sim 1.5$ (Fig. 8b). The total flame length was approximately $15 D_o$. Blue chemiluminescent emission was observed at the flame base with a luminous flame having a length of $\sim 12 D_o$ downstream. These observations imply that partially premixed combustion is dominant at the flame base, while diffusion combustion prevails downstream. In Case 2, the flame is held at $x/D_o \sim 3.5$, which is further downstream of the inner potential core (Fig. 8c). The total flame length was approximately $10 D_o$ and blue chemiluminescent emission was observed at the flame base having a length of $\sim 6 D_o$. Therefore, partially premixed combustion should be dominant in the flame.

Figure 9 shows an instantaneous flame front and the streamwise velocity profiles in the controlled flames. The instantaneous flame front is determined with a thermal boundary between the hot and cold gas, which corresponds to an abrupt decrease in the particle density (Muñiz and Mungal 1997). For both cases, the leading-edge flame is located near the boundary between the outer mixing layer and the static ambient fluid, where the flow velocity is small enough to balance with the flame speed. The leading-edge flame in Case 1 is much closer to the nozzle exit, since the radial transport of the fuel to the outer mixing layer is accomplished more upstream in Case 1 as shown in (A) and (B) in Fig. 6d, h.

In Case 1, the flame fronts at $x/D_o \sim 2$ are far from the jet axis, implying that a great amount of unburnt fuel remains around the jet axis (Fig. 9a). The unburnt fuel is

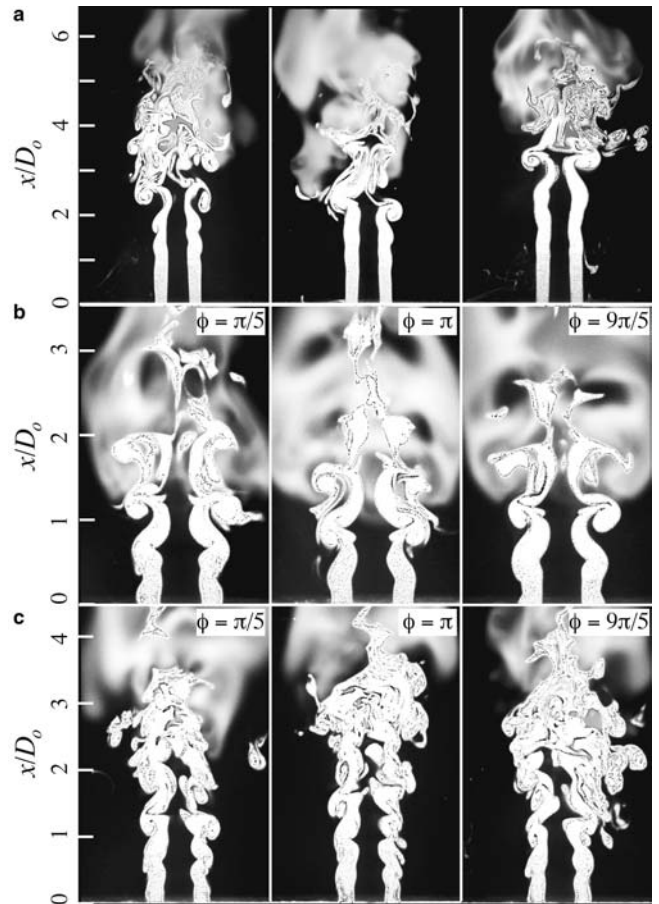


Fig. 8 Instantaneous images of the natural and controlled lifted flames with $St_a = 1.0$. (a) Natural flame, (b) Case 1, and (c) Case 2

likely to be consumed downstream as a diffusion flame with the intense luminescence as described above. On the other hand, in Case 2, the flame fronts at $x/D_o \sim 4$ are closer to the jet axis (Fig. 9b). This is because the annular and central flows are fully merged at the upstream of the flame base as shown in Figs. 5f and 8c, and the flammable region is distributed near the jet axis.

4.2 Blowoff limits

Figure 10 shows the maximum momentum flux ratio m ($= \rho_o U_{m,o}^2 / \rho_i U_{m,i}^2$) for sustaining a stable flame. A lifted flame is deemed stable when it is held at least for 3 min. In the natural flame, the blowoff limit is insensitive to Re , and it ranges from $m = 1.5$ to 2. On the other hand, in the controlled flames, it is significantly extended to larger m for $Re > 2.0 \times 10^3$. The blowoff limit of Case 1 is approximately five times larger than that of the natural flame for $Re = 2.4 \times 10^3$, while that of Case 2 is three times larger.

Stabilization of lifted flames with excitation is previously accomplished using piezoelectric actuators (Chao et al. 2000) or acoustic speaker (Chao and Jeng

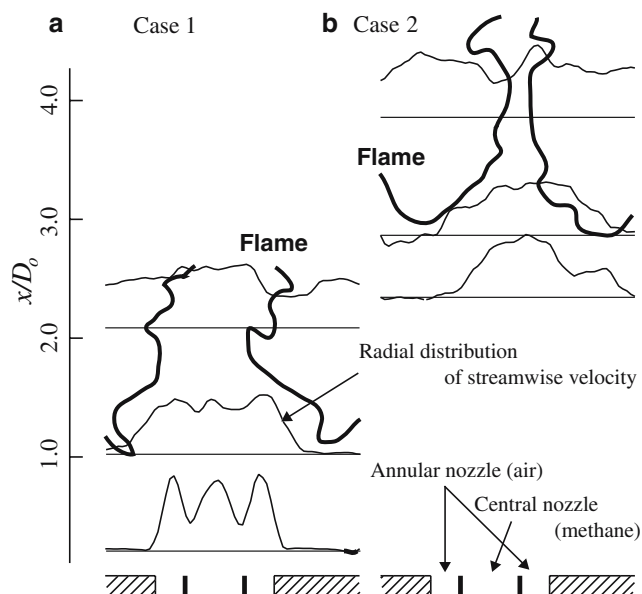


Fig. 9 Instantaneous flame fronts and distributions of the streamwise velocity

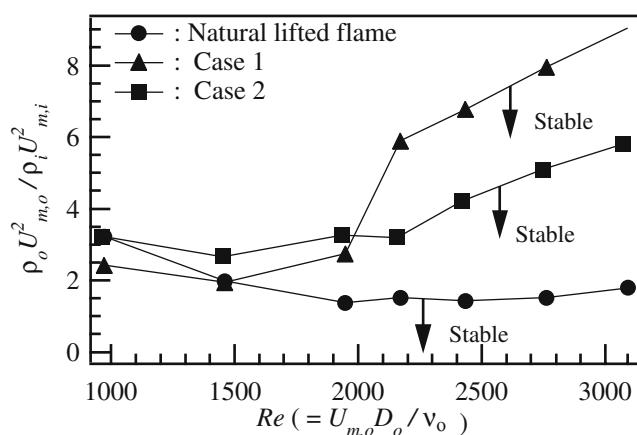


Fig. 10 Blowoff limits of the natural and the controlled flames

1992; Chao et al. 1996, 2002; Baillot and Demare 2002). In their studies, they manipulate lifted flames in the hysteresis region; nozzle exit velocity is relatively small that the natural flame base is held upstream of the jet potential core, and they define the lifted flames as stable when the liftoff height is shortened by excitation. On the other hand, in the present study, the lifted flame is held stably even if the flow velocity is larger than the blowoff limit of the natural flame.

4.3 Exhaust gas assessment

The volumetric fractions of NO_x and CO emission from the natural and controlled flames are shown in Table 1. For the natural flame, the airflow rate is reduced to approximately half that of the controlled flames to keep

Table 1 Overall NO_x and CO emissions of the natural ($U_o = 1$ m/s, $U_i = 1.3$ m/s) and controlled lifted flames ($U_o = 1.8$ m/s, $U_i = 1.3$ m/s)

Component	Natural	Case 1	Case 2
NO_x [ppm at 15% O_2]	82 ± 16	68 ± 10	46 ± 7
CO [ppm at 15% O_2]	380 ± 13	150 ± 10	450 ± 22

the flame stable (Fig. 10). Thus, the data for the natural flames are shown for reference. In the natural flame, both of the NO_x and CO emissions are large. On the other hand, the controlled flames exhibit different trends of emission. The emission of CO for Case 1 is much smaller than that for Case 2, while the NO_x emission for Case 1 is larger than that for Case 2. Correa (1992) reported that the amount of the emissions is sensitive to the local fuel concentration, turbulence characteristics, temperature, and residence time in the flame. With respect to the residence time, it is conjectured that the combustion gas in Case 1 stays in the flame for a longer time, since the flame length of Case 1 is longer than that of Case 2. Consequently, the chemical reactions in Case 1 are presumably more active. Further investigation is necessary to explain detailed mechanisms.

It is now clear that the present control scheme stabilizes the flames, and the flame characteristics are significantly different for Cases 1 and 2. In Sections 4.4 and 4.5, detailed mechanisms of the controlled flames are examined.

4.4 Flame base structures of Case 1

Instantaneous direct images of the flame base for Case 1 are shown in Fig. 11. Both images are acquired at the same control phase of $\phi = \pi/5$. In Fig. 11a, several flame lobes are observed around the outer ridge of the flame base. The flame lobes are considered to be the flame propagating through the flammable mixture trapped in rib structures as shown in Fig. 7 (Demare and Baillot 2001). On the other hand, these lobes are missing at a different instant as shown in Fig. 11b, indicating that they are not periodical structures.

A snap shot of the particle images and the velocity vectors are $(\vec{u}_{\phi=\pi} + \vec{u}')$ shown in Fig. 12. The instantaneous flame front is also depicted as well as the contours of the rich and lean flammable limits of $(\bar{Z} + Z_{\phi=\pi})$ determined from the LIF data of the cold jet. In the particle image, the mean local flame position \bar{h} and its fluctuation $\sqrt{h'^2}$ are depicted. The mean flame positions are $x/D_o = 1.8$ and 1.2, respectively, at $r/D_o = 0.39$ and 0.75, and the magnitude of the fluctuations is comparable to the dimension of the large-scale vortices.

As shown in the velocity field, large-scale vortices are densely populated near the nozzle exit and the flammable mixture is distributed extensively at the flame base (A), ensuring that partially premixed combustion takes place at the location. It is found that the vortical

Fig. 11 Instantaneous images of the controlled flame base with Case 1. Both images are acquired at different instances of $\phi = \pi/5$

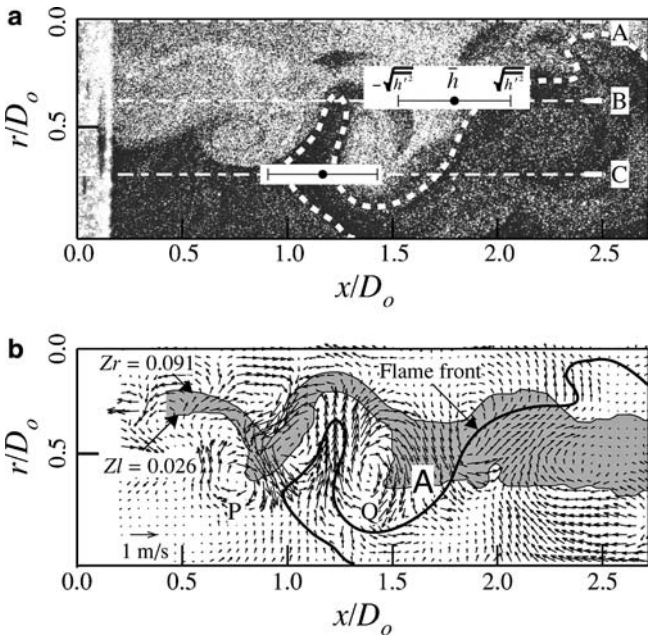
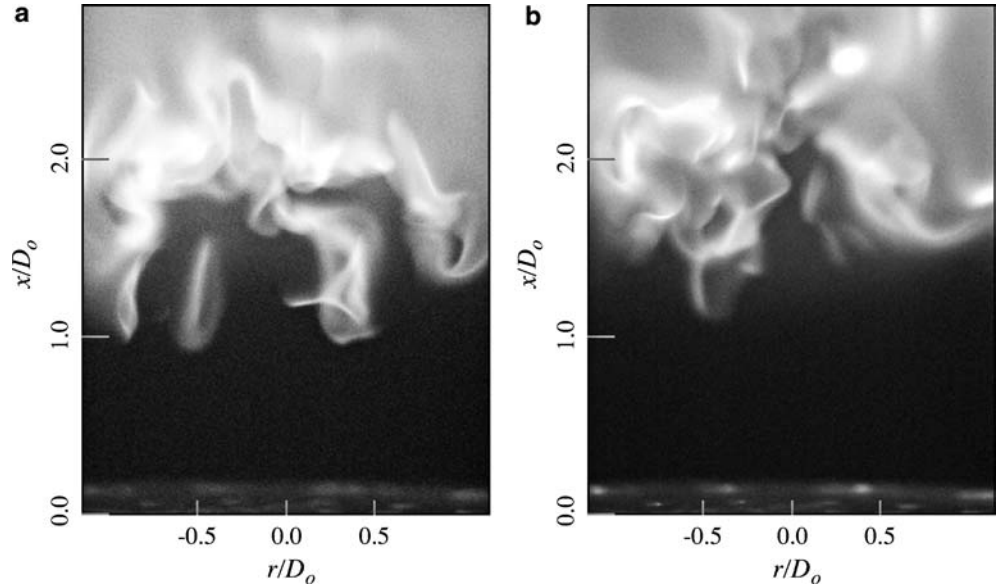


Fig. 12 (a) Instantaneous particle image and (b) velocity vectors ($\vec{u}_{\phi=\pi} + \vec{u}'$) for the controlled lifted flame of Case 1. Instantaneous flame front and contours of rich and lean flammable limits of ($\bar{Z} + Z_{\phi=\pi}$) for the corresponding cold jet are superposed

structures located upstream of the flame base are almost unchanged from those of the cold jet (Fig. 6b).

With respect to the flame front, the leading-edge of the flame is engulfed between the two vortices (P) and (Q). The flame front is considered to be a flame lobe propagating through rib structures as shown in Fig. 11a. Since the rib structures are formed between a pair of large-scale vortices, the flame position is randomly fluctuated with an amplitude of primary vortex diameter as shown in Fig. 12a.

4.5 Distribution of the velocity magnitude

$|\vec{u} + \vec{u}_{\phi=\pi}|$ in the streamwise direction for the cold and flamed jets are shown in Fig. 13. The radial locations are $r/D_o = 0, 0.39$ and 0.75 , which correspond to (A), (B), and (C) in Fig. 12a. At $r/D_o = 0.39$, $|\vec{u}_f|$ is larger than $|\vec{u}_c|$ at $x/D_o > 2$, and the velocity difference continues to increase downstream. Thus, the phase-averaged flame front should be located at $x/D_o \sim 2$, since the velocity difference is likely to be caused by the thermal expansion across the flame front (Muñiz and Mungal 1997). At $r/D_o = 0.75$, the flame front is considered to be at $x/D_o = 1.2$. These estimations of the flame front are in good accordance with the estimates with the instantaneous particle images shown in Fig. 12. On the other hand, along the jet axis, the velocity magnitude of the flamed jet $|\vec{u}_f|$ is in good agreement with that of the cold jet $|\vec{u}_c|$ near the nozzle exit, while $|\vec{u}_f|$ becomes smaller than $|\vec{u}_c|$ at $x/D_o > 1.7$. It is conjectured that the decrease of $|\vec{u}_f|$ is caused by the thermal expansion due to combustion further downstream.

4.6 Stabilization mechanism for Case 1

Instantaneous scalar dissipation rate \tilde{X} is determined with the distribution of the mixture fraction measured in the cold jet. By neglecting variation of \tilde{X} in the azimuthal direction, it is estimated as,

$$\tilde{X} = 2\alpha_1 \left[\left(\frac{\partial \tilde{Z}}{\partial x} \right)^2 + \left(\frac{\partial \tilde{Z}}{\partial r} \right)^2 \right], \quad (5)$$

where $\alpha_1 (= 0.22 \text{ cm}^2/\text{s})$ is the methane diffusivity in air, and \tilde{Z} is the mixture fraction calculated with Eq. 2. The uncertainty interval of \tilde{X} estimated at 95% coverage is 0.4 s^{-1} on the stoichiometric surface. Note that the

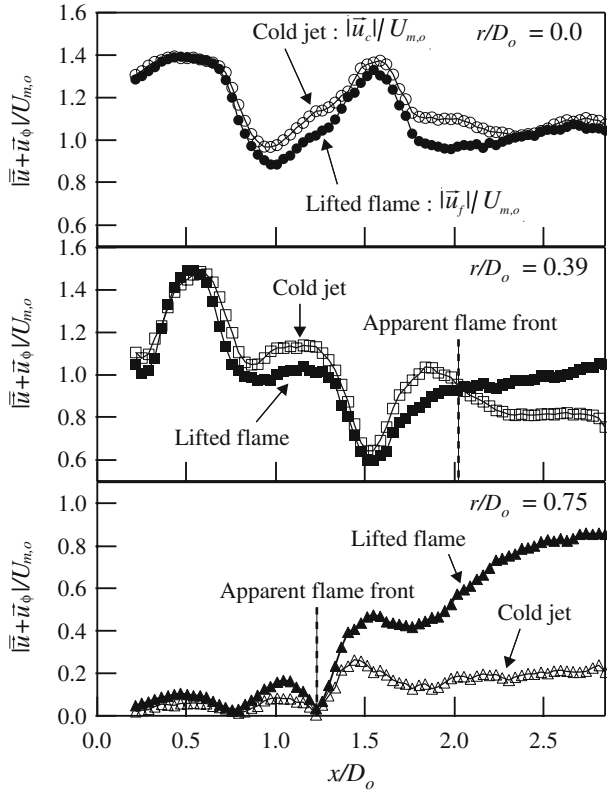


Fig. 13 Axial velocity variation in Case 1 for the controlled lifted flame and the corresponding cold jet

spatial resolution in the present study is $0.4 \times 0.4 \text{ mm}^2$ and the effect of the imperfect resolution on the uncertainty of \tilde{X} is not included. Peters and Williams (1983) show that \tilde{X} at extinction is $X_{\text{qu}} = 5 \text{ s}^{-1}$ in their experiments for methane/air counterflow diffusion flames.

Figure 14 shows instantaneous flammable region determined with PLIF for the cold jet together with contours of \tilde{X} larger than 5 s^{-1} . The flammable layer is significantly distorted by the large-scale vortices in the inner and outer shear layers. In the inner shear layer, the flammable layer becomes thin in the downstream portion of the primary vortex while thick in the upstream portion, which, respectively, correspond to (A) and (B) in the figure. At (A), which approximately corresponds to the position of the lifted flame base, the thinned flammable layer is likely to overlap with the contours of \tilde{X} larger than X_{qu} . This means that diffusion flamelet at the location should be quenched and the flame is not propagated further upstream. Actually, for $0 < r/D_o < 0.5$, the lifted flame base is located at $x/D_o = 1.5 \sim 2.0$, which is at the downstream of (A), as shown in Fig. 12a.

On the other hand, at (B), which is in the upstream portion of the vortex, the flammable layer is thick and \tilde{X} is small enough to allow the flame propagation. As shown in (B), (C), and (D), the flammable layer becomes thicker as the induced vortex breaks down into turbulence. At $\phi = 13\pi/5$, the flammable mixture is distributed extensively at $x/D_o = 1.5 \sim 2.0$.

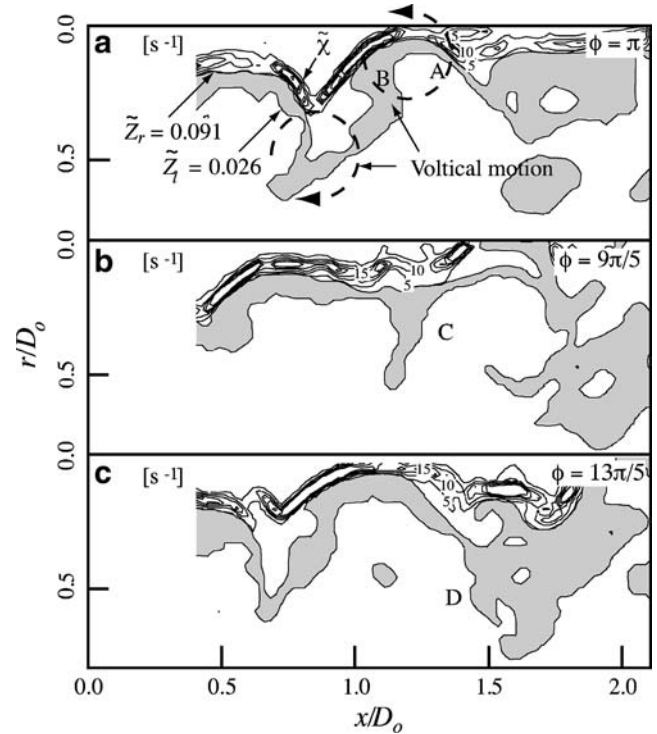


Fig. 14 Instantaneous contours of the rich and lean flammable limits of the mixture fraction \tilde{Z} for the controlled cold jet of Case 1. Contours of the scalar dissipation rate \tilde{X} larger than the extinction value of $X_{\text{qu}} = 5 \text{ s}^{-1}$ estimated by Peters and Williams (1983) are overlaid

Therefore, one cycle of the flame propagation is considered as follows: first, the flame should be held at the downstream of (A) at $\phi = \pi$. Then, the dissipation rate is weakened at $\phi = 9\pi/5$, and the flame propagates upstream to ignite the thickened flammable layer formed at $\phi = 13\pi/5$. Last, the flame continues to propagate upstream until it is quenched by the excessive dissipation rate at $\phi = \pi$.

Ashurst and Williams (1990), Everest et al. (1996), and Chao et al. (2002) show that extensive strain makes the flammable layer thinner with large dissipation rate at the downstream part of the large-scale vortex, and causes the flame extinction, while, in the upstream region, compressive strain makes the flammable layer thicker with small dissipation rate, which allows the flame propagation. Our experimental data for the manipulated methane/air coaxial lifted flame are in good agreement with their findings.

Figure 15 shows the spatio-temporal evolution of the velocity vectors $(\bar{u} + \bar{u}_\phi)$, phase-averaged flame front, and the rich and lean flammable limits calculated from $(\bar{Z} + Z_\phi)$. It is found that the flammable layer formed in the upstream part of the primary vortex becomes thicker as the vortex breaks down into turbulence, and the flame base is provided with the flammable mixture periodically at the flapping frequency f_a .

The leading-edge of the phase-averaged flame is considered to be a flame lobe which propagates the

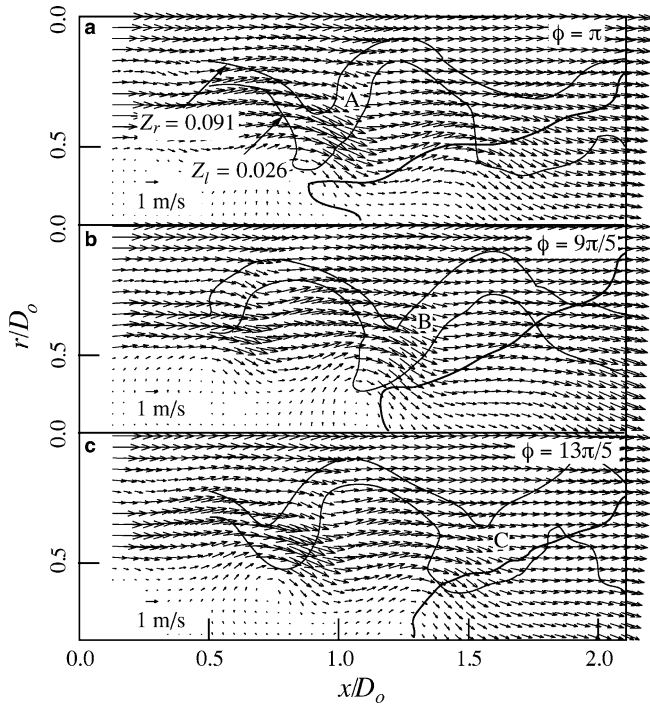


Fig. 15 Spatio-temporal evolution of velocity vectors ($\bar{\mathbf{u}} + \bar{\mathbf{u}}_\phi$) for the controlled lifted flame of Case 1. Phase-averaged flame fronts and contours of the rich and lean flammable limits of ($\bar{Z} + Z_\phi$) for the corresponding cold jet are overlaid

premixure trapped in rib structures as discussed in Figs. 11 and 12. It is found that the leading-edge flame is not superimposed on the flammable layer. Two possible reasons should be considered. First, the rib structures emerge randomly, so that the flammable layer associated with them is smeared out in the phase-averaged field, whereas the phase-averaged flame is captured at the same location with the velocity difference between the flamed and cold flows. Second, the present flame detection scheme has substantial error in the flame location where the thermal expansion is vigorous. Further analysis is necessary to examine the discrepancy.

Since partially premixed combustion is dominant at the flame base, the flame speed S_T should balance with the local flow velocity. At $\phi = 13\pi/5$, as shown in Fig. 14c, the flammable mixture is distributed extensively due to the breakdown of the induced vortex and the flame should propagate the thickened flammable layer upstream. In order to estimate S_T at $\phi = 13\pi/5$, a conditional-average of the velocity vectors right upstream of the flame front overlapping with the flammable layer is made. Linear interpolation is used to compute velocity at the flame front. As shown in Fig. 16, the flame front leans to the jet axis by 23° . Since the flame speed S_T balances with the velocity component \bar{u}_n normal to the flame front, S_T equals the magnitude of \bar{u}_n . Assuming that S_T is constant over the flame base, S_T thus estimated is 0.66 m/s, which is 1.8 times of the maximum laminar flame speed for methane/air premixed flame, $S_L = 0.38$ m/s (Muñiz and Mungal 1997). The

estimate $S_T = 1.8 S_L$ is consistent with the result of Muñiz and Mungal (1997) that the flame speed at the lifted flame base is smaller than $3 S_L$.

In order to clarify the reason why the lifted flame is stabilized when controlled with $St_a = f_a D_o / U_{m,o} = 1.0$, Damköhler number D_a is defined as follows:

$$D_a = \frac{1/f_a}{l_F/S_T}, \quad (6)$$

where l_F is the mean width of the thickened flammable layer in a direction normal to the flame front, and is approximately $0.3 D_o$ at $\phi = 13\pi/5$. The Damköhler number D_a thus defined corresponds to a ratio between the formation period of the thickened flammable layer and the time necessary for the premixture to be burnt. For $St_a = 1.0$, D_a is estimated to be 1.1. Therefore, the formation period of the thickened flammable layer is balanced with its consumption time, and the flame becomes stable since the ignition of the thickened flammable layer of the following primary vortex is certainly ensured. On the other hand, for $St_a = 0.3$, D_a becomes as large as 3.8, and the flame is unstable and easily blows off.

4.7 Flame base structures of Case 2

Figure 17 shows a snap shot of the particle images and the velocity vectors ($\bar{\mathbf{u}}_{\phi=\pi} + \bar{\mathbf{u}}'$) in Case 2. The instantaneous flame front and the contours of $Z_r = 0.091$ and $Z_l = 0.026$ are also depicted. The averaged flammable mixture is distributed close to the jet axis due to the vigorous mixing upstream, which is consistent with the conjecture in Section 4.1 that partially premixed combustion prevails. The flame speed should thus balance with the local flow velocity. In the particle image, the mean and fluctuation of the local flame positions are depicted as \bar{h} and $\sqrt{h'^2}$, respectively. The fluctuation is relatively small over all radial locations examined. Unlike in Case 1, large-scale intense vortices are absent, because those vortices are broken down into turbulence upstream as shown in Fig. 6. Therefore, in Case 2, the flame is stabilized due to the small velocity fluctuations near the flame base.

Figure 18 shows the probability density function (PDF) of the streamwise velocity in the inner mixing layer (Station D in Fig. 17), which is obtained from 200 instantaneous PIV images. The PDF in the natural and controlled cold jets with $St_a = 0.3$, where flames are unstable and easily blow off, are also depicted. In those unstable flames, there are several peaks in PDF over a broad range of velocity. These peaks are due to the passage of the large-scale vortical structures having intense velocity fluctuations. It is conjectured that these intense fluctuations disturb steady flame propagation, and the flames become unstable. On the other hand, in the controlled stable flame with $St_a = 1.0$, the velocity fluctuation is smaller, and the PDF is distributed in a narrow range and has only one peak at 1.7 m/s.

Fig. 16 Estimate of the flame speed at the lifted flame base controlled with Case 1

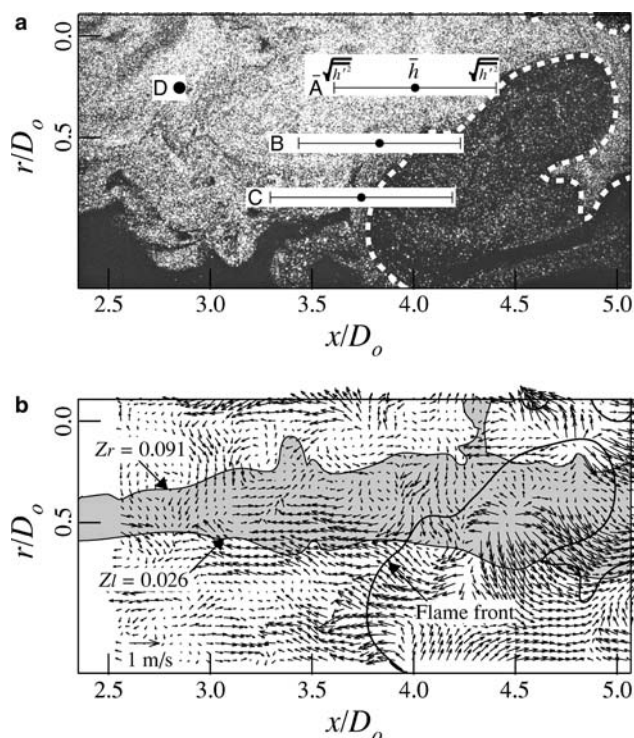
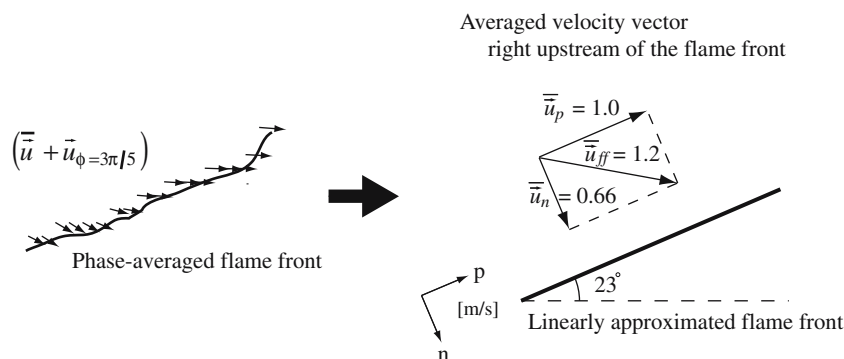


Fig. 17 (a) Instantaneous particle image and (b) velocity vectors ($\bar{u}_{\phi=\pi} + \bar{u}'$) for the controlled lifted flame of Case 2. Instantaneous flame front and contours of rich and lean flammable limits of ($Z + Z_{\phi=\pi}$) for the corresponding cold jet are superposed

5 Conclusions

Active control of a lifted flame using arrayed micro flap actuators is investigated. We successfully manipulate the flame characteristics such as liftoff height, blowoff limit, and emission trend by introducing disturbances directly into the initial shear layers by the flaps. Spatio-temporal evolution of large-scale vortical structures is examined with the aid of PIV and PLIF in order to elucidate the control mechanisms. Dependent on the driving signal of the flaps, the near-field vortical structures are significantly modified and two types of lifted flames having different stabilization mechanisms are realized.

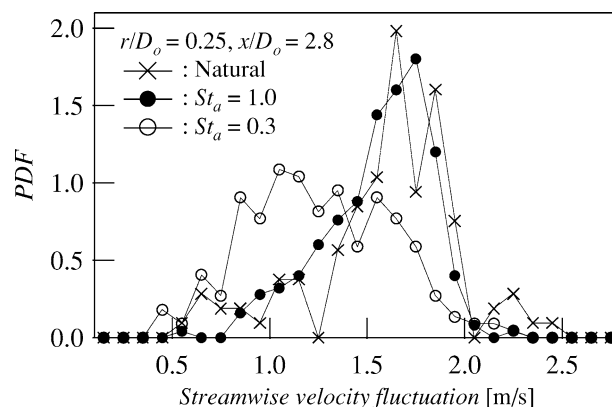


Fig. 18 The PDF of the streamwise velocity fluctuation for Case 2 in the inner mixing layer upstream of the flame base

When the flap motion with the saw-wave signal is introduced into the outer shear layer, large-scale intense vortices are induced in phase with the signal. When the flapping Strouhal number is unity, the controlled lifted flame becomes stable and the blowoff limit is extended significantly. The flame base is anchored at $x/D_o \sim 1.5$, since the induced vortex transports the inner fuel to the outer mixing layer near the nozzle exit, where the flow velocity is small enough to allow the flame propagation. It is found for $St_a = 1.0$ that the formation period of the flammable layer in the upstream part of the vortex is in good agreement with the time necessary for the premixture to be burnt at the flame base. This balance between supply and consumption should contribute to the flame stabilization mechanism.

On the other hand, when the jet is manipulated with the flap motion with the square-wave signal, vortices breakdown into turbulence near the nozzle exit, and the flame is held stably at $x/D_o \sim 4$, which is downstream of the inner potential core. The flame is stabilized, because the steady flame propagation is ensured due to the smaller velocity fluctuation near the flame base.

Acknowledgments This work was supported through the research project on Micro Gas Turbine/Fuel Cell Hybrid-Type Distributed Energy System by the Department of Core Research for Evolutional Science and Technology (CREST) of the Japan Science and Technology Corporation (JST).

References

- ANSI/ASME PTC 19.1 (1985) Measurement uncertainty. Supplement on instruments and apparatus, part 1, ASME
- Ashurst WT, Williams FA (1990) Vortex modification of diffusion flamelets. The 23rd International Symposium on Combustion, pp543–550
- Baillet F, Demare D (2002) Physical mechanisms of a lifted non-premixed flame stabilized in an acoustic field. *Combust Sci Tech* 174:73–98
- Cantwell BJ (1981) Organized motion of turbulent-flow. *Ann Rev Fluid Mech* 13:457–515
- Chao YC, Jeng MS (1992) Behavior of the lifted jet flame under acoustic excitation. In: Proceedings of the 24th International Symposium on Combustion, pp 333–340
- Chao YC, Yuan T, Tseng CS (1996) Effect of flame lifting and acoustic excitation on the reduction of NO_x emissions. *Combust Sci Tech* 113:49–65
- Chao YC, Jong YC, Sheu HW (2000) Helical-mode excitation of lifted flames using piezoelectric actuators. *Exp Fluids* 28:11–20
- Chao YC, Wu CY, Yuan AT (2002) Stabilization process of a lifted flame tuned by acoustic excitation. *Combust Sci Tech* 174:87–110
- Correa SM (1992) A review of NO_x formation under gas turbine combustion conditions. *Combust Sci Tech* 87:329–362
- Crow SC, Champagne FH (1971) Orderly structure in jet turbulence. *J Fluid Mech* 48:547–591
- Dahm WJA, Frierler CE, Tryggvason G (1992) Vortex structure and dynamics in the near field of a coaxial jet. *J Fluid Mech* 241:371–402
- Demare D, Baillet F (2001) The role of secondary instabilities in the stabilization of a nonpremixed lifted flame. *Phys Fluids* 13:2662–2670
- Drake MC, Correa SM, Pitz RW, Shyy W, Fenimore CP (1987) Superequilibrium and thermal nitric oxide formation in turbulent diffusion flames. *Combust Flame* 69:347–365
- Everest DA, Feikema DA, Driscoll JF (1996) Images of the strained flammable layer used to study the liftoff turbulent jet flames. The 26th International Symposium on Combustion, pp 129–136
- Favre-Marinet M, Camano Schettini EB (2001) The density field of coaxial jets with large velocity ratio and large density differences. *Int J Heat Mass Trans* 44:1913–1924
- Fujimori T, Riechelmann D, Sato J (1998) Effect of liftoff on NO_x emission of turbulent jet flame in high-temperature coflowing air. The 27th International Symposium on Combustion, pp 1149–1155
- Ho CM, Huerre P (1984) Perturbed free shear layers. *Ann Rev Fluid Mech* 16:365–424
- Ho CM, Tai YC (1996) Review: MEMS and its applications for flow control. *ASME Int Fluids Eng* 118:437–447
- Hussain AKMF, Zaman KBMQ (1981) The preferred mode of the axisymmetric mode. *J Fluid Mech* 110:39–71
- Kean RD, Adrian RJ (1990) Optimization of particle image velocimeters. Part I: Double pulsed systems. *Meas Sci Technol* 1:1202–1215
- Kean RD, Adrian RJ (1992) Theory of cross-correlation analysis of PIV images. *J Appl Sci Res* 49:191–215
- Kurimoto N, Suzuki Y, Kasagi N (2001) Active control of coaxial jet mixing and combustion with arrayed micro actuators. In: Proceedings of the fifth World Conference on Experimental Heat Transfer, Fluid Mechanics and Thermodynamics, Thessaloniki, pp 511–516
- Liepmann D, Gharib M (1992) The role of streamwise vorticity in the near-field entrainment of round jets. *J Fluid Mech* 245:643–668
- Lozano A, Yip B, Hanson RK (1992) Acetone: a tracer for concentration measurements in gaseous flows by planar laser-induced fluorescence. *Exp Fluids* 13:369–376
- Melling A (1997) Tracer particles and seeding for particle image velocimetry. *Meas Sci Technol* 8:1406–1416
- Muñiz L, Mungal MG (1997) Instantaneous flame-stabilization velocities in lifted-jet diffusion flames. *Combust Flame* 111:16–31
- Peters N, Williams FA (1983) Liftoff characteristics of turbulent jet diffusion flames. *AIAA J* 21:423–429
- Pitts WM (1988) Assessment of theories for the behavior and blowout of lifted turbulent jet diffusion flames. The 22nd International Symposium on Combustion, pp 809–816
- Rehab H, Villermaux E, Hopfinger EJ (1997) Flow regimes of large-velocity-ratio coaxial jets. *J Fluid Mech* 345:357–381
- Schefer RW, Goix PJ (1998) Mechanism of flame stabilization in turbulent lifted-jet flames. *Combust Flame* 112:559–574
- Su LK, Han D, Mungal MG (2000) Measurements of velocity and fuel concentration in the stabilization region of lifted jet diffusion flames. *Proc Combust Inst* 28:327–334
- Suzuki H, Kasagi N, Suzuki Y (1999) Manipulation of a round jet with electromagnetic flap actuators. In: Proceedings of the 12th IEEE International Conference on MEMS'99, Orlando, pp 534–540
- Suzuki H, Kasagi N, Suzuki Y (2004) Active control of an axisymmetric jet with distributed electromagnetic flap actuators. *Exp Fluids* 36:498–509
- Uechi H, Kimijima S, Kasagi N (2004) Cycle analysis of gas turbine-fuel cell cycle hybrid micro generation system. *J Eng Gas Turbines Power* 126:755–762
- Vanquickenborne L, Tiggelen AV (1966) The stabilization mechanism of lifted diffusion flames. *Combust Flame* 10:59–69
- Vervisch L (2000) Using numerics to help the understanding of non-premixed turbulent flames. *Proc Combust Inst* 28:11–24
- Zaman KBMQ, Hussain AKMF (1980) Vortex pairing in a circular jet under controlled excitation. *J Fluid Mech* 101:449–491